J Nanopart Res (2022) 24:249
https://doi.org/10.1007/s11051-022-05612-2

RESEARCH PAPER

Novel concept on in situ syntheses and investigation of photon energy effect on AgNP size with a custom build device for enhanced antimicrobial efficiency

Ulviye Bunyatova · Ismail Cengiz Kocum · Kubra Erkan Turkmen · Orhan Erdem Haberal · Onur Kocak · Helin Cikmaz Koca

Received: 9 August 2022 / Accepted: 31 October 2022 / Published online: 28 November 2022

Abstract The objectives of the present study were to examine the influence of visible light photons on photoreduction of the silver nanoparticles (AgNPs), detect optoelectronic feedback, and observe the antimicrobial activity. For this purpose, an optoelectronic device was designed and successfully tested. The finding shows that identical nanocomplexes with silver salt express various responses to the LEDs with different wavelengths by scattering different portions of light. It is the first time to discuss the effect of visible light photons on nano-sized particles in detail based on the quantitative optical/voltage analysis. The photoreduction of the AgNPs is in good agreement with photon energy and the AgNPs occur in nanocomplex in a wavelength versus time-dependent manner. The blue LED having photon energy 7.04 eV reduces the average size of AgNPs down to the range 4–6 nm in 12 min, while AgNPs obtained under influence of green (6.11 eV) and red (5.04 eV) LEDs have average sizes 6–8 nm and 12–14 nm respectively. The successful synthesis of AgNPs was additionally examined using UV–Vis, SEM, XPS, XRD, FTIR, and TEM techniques. AgNPs proved for antimicrobial activity against *Escherichia coli* 25922, *Enterococcus faecalis* 29212, *Pseudomonas aeruginosa* 27853, and *Candida albicans* 10231 at four different concentrations. The antibacterial test for all selected bacteria showed that AgNPs which have an average size of 4-6 nm synthesized by blue LED revealed the largest inhibition zone around 16–11 mm, while the antifungal test shows that the maximum inhibition zone was exposed by AgNPs which have an average size of 6–8 nm synthesized by red LED.

Keywords Silver nanoparticles · Bionanocomposites · LED-driven AgNPs · Visible light-sensitive optoelectronic circuit · Antimicrobial activity

JEL Classification 2.01 · 2.04 · 4.02 · 5.11 · 6.03

Topical Collection on *Nanoarchitectonics for Functional Particles and Materials*.

U. Bunyatova (✉) · I. C. Kocum · O. E. Haberal · O. Kocak · H. C. Koca
Biomedical Department, Baskent University, Engineering Facility, Ankara 06790, Turkey
e-mail: bunyatovau@yahoo.com

K. E. Turkmen
Faculty of Science, Department of Biology, Karamanoglu Mehmetbey University, 70200 Karaman, Turkey

K. E. Turkmen
Department of Biology, Division of Biotechnology, Hacettepe University, 06800 Ankara, Turkey

Introduction

Metallic nanoparticles are used in a wide range of applications in biomedical applications and achieved great success in diagnosis, anticancer treatment, gene, and drug delivery [1–4]. In recent years various

synthetic methods have been developed for the manufacture of metal nanoparticles (Au, Ag, Zn, Cu, etc.), which include thermal decomposition [5], sonochemical synthesis [6], chemical reduction [7], laser ablation [8], and biomimetic synthesis [9]. The preparation of metal NPs by bio-reduction [10] and extracellular biosynthesis [11] methods were also reported. Metallic antimicrobial agents play an essential role in the control of infectious diseases and in preventing spread of pathogens. Metal nanoparticles, such as copper, gold, and silver, can be extremely toxic to bacteria at exceptionally low concentrations and are able to have prolonged activity due to the slow release of their cations in living media [12–14].

Ag salts have been noticed since antiquity because of their antibacterial effects and are now among the most attractive nanomaterials. Silver nanoparticles (AgNPs) are widely used in therapeutics, biotechnology, medical device coatings, personal health care, and antimicrobial and anticancer treatments [15–17]. It is obvious that for medicinal applications NPs need to have the biocompatible capacity, which is usually obtained green protocols or non-toxic environmentally friendly encapsulating approaches.

It is known that the functional groups such as hydroxyl, carboxyl, and amine, are reductive in the presence of light [18–20]. Despite the photo-mediated syntheses of metal nanostructures being an active and well-known area of research [21–24], there is no other instance visible light photo-activated synthesis of AgNPs by the harmless visible light source, except ours [4, 6]. AgNPs strongly absorb visible light due to the localized surface plasmon resonance (LSPR) effect around 400–425 nm. A distinct benefit of silver NPs is that its light absorption is not limited to a certain wavelength but instead they are able to utilize a broad range of wavelengths; literature reports demonstrate that the light absorption, scattering, and excitation responses of noble NPs strongly depend on the shape, size, and particle–particle interactions [24–26]. The photon causes an electron to become "excited" in these functional groups. This action depends on the wavelength of photons, which is an important property of light and determines its nature and energy as well as its behavior with the surrounding environment.

In this study, our goal was to design and test a harmless apparatus for reducing biocompatible AgNPs in biopolymer composite, detecting optoelectronic feedback and observing the antimicrobial activity.

Our study was motivated by the importance of finding an effective way for obtaining biocompatible and antimicrobial AgNPs by using eco-friendly and harmless visible light irradiation, as well as its relatively low cost with other nanoparticle fabrication methods [5–11]. The novelty of this device was that it can utilize scattering light for real-time monitoring and quantifying the formation process of AgNPs. To the best of our capacity, the scattering light has never been achieved previously in monitoring and quantifying the formation process of AgNPs. Within visible light stimulation, AgNPs in nanocomposite blend grow gradually and biopolymer composite forms a stable protection layer on the AgNP surface. The antimicrobial activity of these AgNPs was performed against *E. coli 25,922*, *E. faecalis 29212*, *P. aeruginosa 27,853*, and *C. albicans 10,231*. Obtained findings evidenced good antimicrobial ability and potential disinfection properties of these particles in addition to their visible light sensitivity. These findings not only contribute to proving the capability of our novel approach but also envisaging the prospective future use of these particles for biomedical applications as well as wastewater treatment, where both bacteria and yeast might be present.

Experimental part

Instrumental part

To produce 3 different wavelengths, harmless radiation a custom device was constructed. This device contains both electronic and mechanical parts and has been designed for this particular purpose. (Fig. 1) For that reason, this simple and cost-effective device is briefly explained as follows: several LEDs (red, green, blue) with ultrabright and mid-power (0.5 W) (AVAGO Technologies, USA) were selected in the visible spectrum for stimulation photoreaction in a nanocomposite solution. During the reaction, observation of both transmittance and scattering were recorded by two photodiodes.

As it is known, each color of LED consists of different doped materials. For that reason, each color

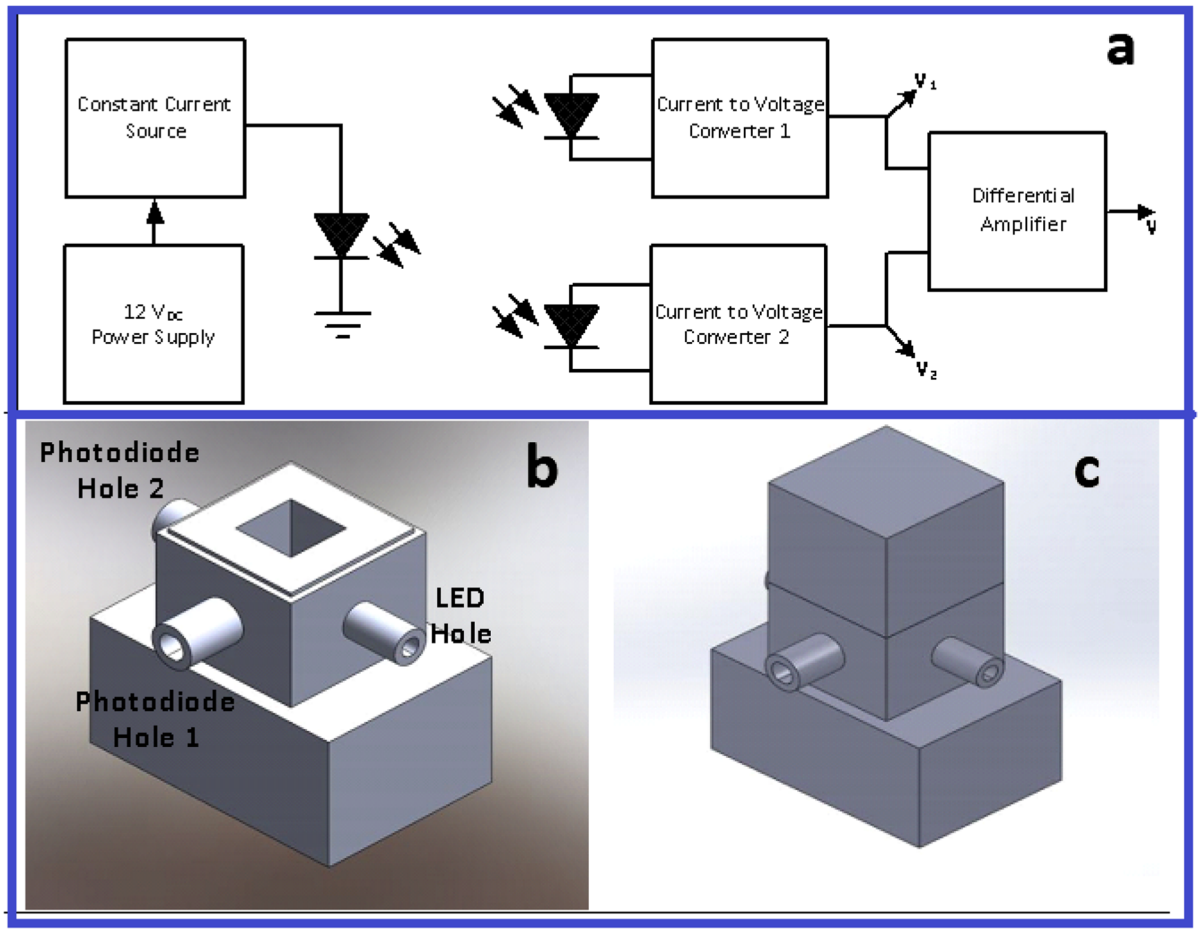

Fig. 1 **a** Custom designed device block diagram; two I/V (current to voltage) converter and a differential amplifier were used for intensity detection. **b** Designed and printed optical black box. During the reaction, scattering photons were recorded by the photodiode fixed in hole1, while transmitted photons were collected by the photodiode in hole 2; **c** a black box with a cuvette inside (not seen in the picture)

of LED has different efficiencies and has different light intensities for the same driving current. Thus, before this study, chosen colors of LEDs (red, green, blue) were tested under a spectrometer (Thorlabs FTS CCS100). By using a constant current source which is made in our laboratory, the intensity of each color was recorded for different current values of 5, 10, 15, 20, 30, 40, and 50 mA respectively. In this way, for the same intensity level, the driving current values of each LED have been determined, and presented in Table 1. After that, all the studies were carried out under the same intensity level, but different current values were determined for this intensity of each color.

Table 1 The driving current values of blue, green, and red LEDs at the same value of intensity

LED	Current (mA)	Wavelength (nm)	Intensity arbitrary unit (a.u.)
Blue	10	450	0.6
Green	50	525	0.6
Red	30	630	0.6

Materials and methods

Silver nitrate, $AgNO_3$, carboxymethyl cellulose (afterward CMC), poly (acrylic acid-co-maleic acid

(MA), and octadecyl amine montmorline ODA-MMT were obtained from Sigma-Aldrich. $AgNO_3$ in carboxymethyl cellulose_ ODA/MMT_ poly (acrylic acid-co-maleic acid) aqueous complex was mixed as described previously [4]. Briefly, 0.8 mL of 9% aqueous CMC & 0.05% ODA_MMT suspension and 0.2 mL of 20% of an aqueous solution of MA were mixed and afterward 10 mg of silver nitrate ($AgNO_3$) was added and stirred at room temperature for 1 h. All experiments involving irradiation of nanocomposites were performed by employing 3 different blue-LED (450 nm), green-LED (525 nm), and red-LED (630 nm) light sources for certain time intervals using the produced custom device.

The nanocomposite specimen preparation procedure and analysis methods

For SEM and XRD examinations, cast films and powered samples were used respectively.

Irradiated three different LED nanocomposites were cast on a glass surface using the applicator and stored in a vacuum oven overnight at 20 °C. Obtained films were used for SEM studies. For XRD examination those films were powered.

For FTIR, UV–vis, and TEM, a fresh hydrogel sample was used. The concentration of samples for FTIR and UV–vis was adjusted to around 0.1%. For TEM examination, a drop of extra diluted (0.01%) nanocomposite solution was placed onto the carbon-coated copper grid and followed by evaporation at room temperature overnight. In this case, the thinly sliced sample was obtained.

In order to define the surface morphology of AgNP nanocomposites, scanning electron microscope SEM-ZEISS EVO 40 with EDS detector and 500 V–30 kV power were used. Before performing the examination by SEM, the cast film samples were coated with a thin gold layer.

In XRD patterns and X-ray reflection parameters, the PANANALYTICAL X-ray powder diffractometer (XRD) with CuKa tube and Ni filter (l = 1.5406 Å) was used for the examination of the physical structure of nanocomposites. The XRD patterns and X-ray reflection parameters were measured at (2θ) angles in the range of 1–90°. For XRD examination, powered samples were used.

UV–Vis measurements were obtained with the Agilent 8453 UV–visible Spectroscopy System using a 1-cm path lengthquartz cell. For the blank sample, distilled water was used. The spectrum of baseline was recorded between 200 and 800 nm. Specimen tests were performed at standard mode the same orientation as for the reference measurement (about 3 ml of the fresh diluted nanocomposite sample was filled into the cell).

Fourier transform infrared (FT-IR) spectroscopy was performed by means of VERTEX 80/80v FTIR spectrometer, in the range between 400 and 4000 cm^{-1} with a resolution of 4 cm^{-1}. A drop of distilled water was run as a pure solvent for a baseline. Then a small drop of diluted hydrogel was placed on plates and runs for test.

In the transmission electron microscopy (TEM), the internal morphology, nano-sizes, and diameter distributions of silver AgNPs in nanocomposites were performed by FEI Technai G2 S-Twin Transmission Electron Microscopy with an accelerating voltage between 120 and 200 kV. In this case, the thinly sliced sample on the carbon-coated copper grid was used.

Antimicrobial activity tests

The disc-diffusion method was used to evaluate the antifungal and antibacterial activity of AgNPs. For this purpose, *E. coli* 25922, *E. faecalis* 29212, and *P. aeruginosa* 27853 were cultured in Luria Bertani (LB, Merck Co., Darmstadt, Germany) broth medium for 37 °C at 24 h. Also, *C. albicans* 10231 was cultured in Sabouraud Dextrose Broth (SDB, Merck Co., Darmstadt, Germany) medium for 24 h at 37 °C. Subsequently, the turbidity of all cultures was adjusted to 0.5 McFarland value. The microorganism's suspensions were inoculated as 100 µL onto Mueller–Hinton Agar (MHA, Oxoid, Co., Wesel, Germany) medium. Sterile paper discs (6 mm in diameter, Bioanalyse, Turkey) were placed on MHA, and each paper disc was impregnated with 20 µL volumes of different concentrations of AgNPs. All inoculated plates were incubated at 37 °C for 24 and 48 h. For the calculation of the antimicrobial effect of AgNPs, inhibition zone diameters were measured after incubation. Nanocomposite samples irradiated by green LED were denoted as "sample 1-S1," sample irradiated by blue LED as "sample 2-S2," and sample irradiated by red LED as "sample 3-S3."

Statistical evaluation

All experiments were conducted at least three times. The data are shown as mean ± standard deviation. A one-way analysis of variance (ANOVA) was used to compare the treatments and $p < 0.05$ was considered significant. The statistical analysis of the data was performed using MATLAB (The Math Works, Inc. MATLAB. Version 2021b).

Results and discussion

Photogeneration of AgNPs by blue, green, and red LEDs

Three mixtures with identical concentrations of components, prepared according to the above-mentioned procedure, have been exposed accordingly blue LED, green LED, and red LED irradiation for certain time intervals. The colloidal soft sample in 1-cm quartz cuvette was placed inside of the black box (Fig. 1b, c) and V circuit's voltage output were recorded. The optical voltage signal from the Rayleigh scattering was recorded at photodiode 1 and the transmitted light signal was received at photodiode 2.

Morphological, structural, and optical characterizations

İrradiated nanocomposites were examined for detecting internal and external morphological characterization using TEM, SEM, XPS, FTIR, XRD, and UV–vis techniques.

TEM images reveal that AgNPs obtained by stimulation of different wavelength LEDs show quasi-spherical shaped nanoparticles (Fig. 2a–f). Images a, d, and f were analyzed by ImageJ software and corresponding particle size distribution histograms are shown in g, h, and i respectively. Histograms for AgNPs possess an average size distribution between 4–6 nm (2 g), 6–8 nm (2 h), and 12–14 nm (2i) obtained under irradiation by blue LED, green LED, and red LED respectively. TEM images showed relatively good, dispersed distribution of AgNPs. Similar TEM images were reported for extra small AgNPs obtained by irradiation 350-nm wavelength UV light [27] and fluorescent silver nanoparticles [28].

SEM images (Fig. 3) show that the extra small nanoparticles in the hydrogel matrix encapsulated onto hybrid porously structured hydrogel. This hydrogel composite prevents the further agglomeration of Ag nanoparticles. Red arrowheads indicate encapsulated AgNPs on the surface studied hybrid nanocomposite film. Due to the 2 (Ag) to 98 w/w ratio of silver to nanocomposite polymer weight SEM images reveal a whole polymer matrix with poor distributed AgNPs. The EDS results show strong carbon peaks along a relatively weak silver signal (Fig. 4b). EDS map spectrum exhibits a characteristic signal of silver element at 3 keV which confirms the formation of silver nanoparticles [29]. The weakness of intensity at 3 keV can be explained by the low initial concentration (2%w/w) of silver ions in the nanocomposite blend. The highest sharp peak corresponds to the energy peak of the carbon, which is in agreement with the highest proportion of the used biopolymer (98% w/w) in the hybrid nanocomposite blend.

Formation of AgNPs within a bionanocomposite matrix was further evidenced by XRD and UV–Vis analysis (Fig. 4). X-ray diffraction patterns are given at Fig. 4 for all light-irradiated nanocomposites. For blue LED-irradiated nanocomposite (Fig. 4a), the Bragg reflection peaks were observed at 2θ values of 27.78°, 32.19°, 38.12, and 46.13 which are indexed to (111), (200), (111), and (200) planes of pure silver based on the face-centered cubic structure. The green and red LED-irradiated nanocomposites (Fig. 4b, c) show an almost identical pattern with the same numbers of Bragg reflection peaks observed at the following 2θ values:27.78°, 32.19°, 38.12, 46.13°, and 64.42 with the corresponding hkl values (111), (200), (111), (200), and (220), respectively, and designates the face-centered-cubic (fcc) AgNPs and signifies the crystalline nature of the studied AgNPs [30–32].

The weakness of intensity detected diffraction peaks can be explained by the low concentration (2%w/w) of silver ions in the nanocomposite blend (please see EDS map Fig. 3]. Similar results were observed in [33] for reflections intensities of 111, 200, 220, and 311 silver crystals and (111), and (200) planes [34]. These reports confirm that silver crystalline reflections decrease with decreasing AgNO3 concentrations in polymer composite. The broad peak observed at all XRD patterns with the maximum at

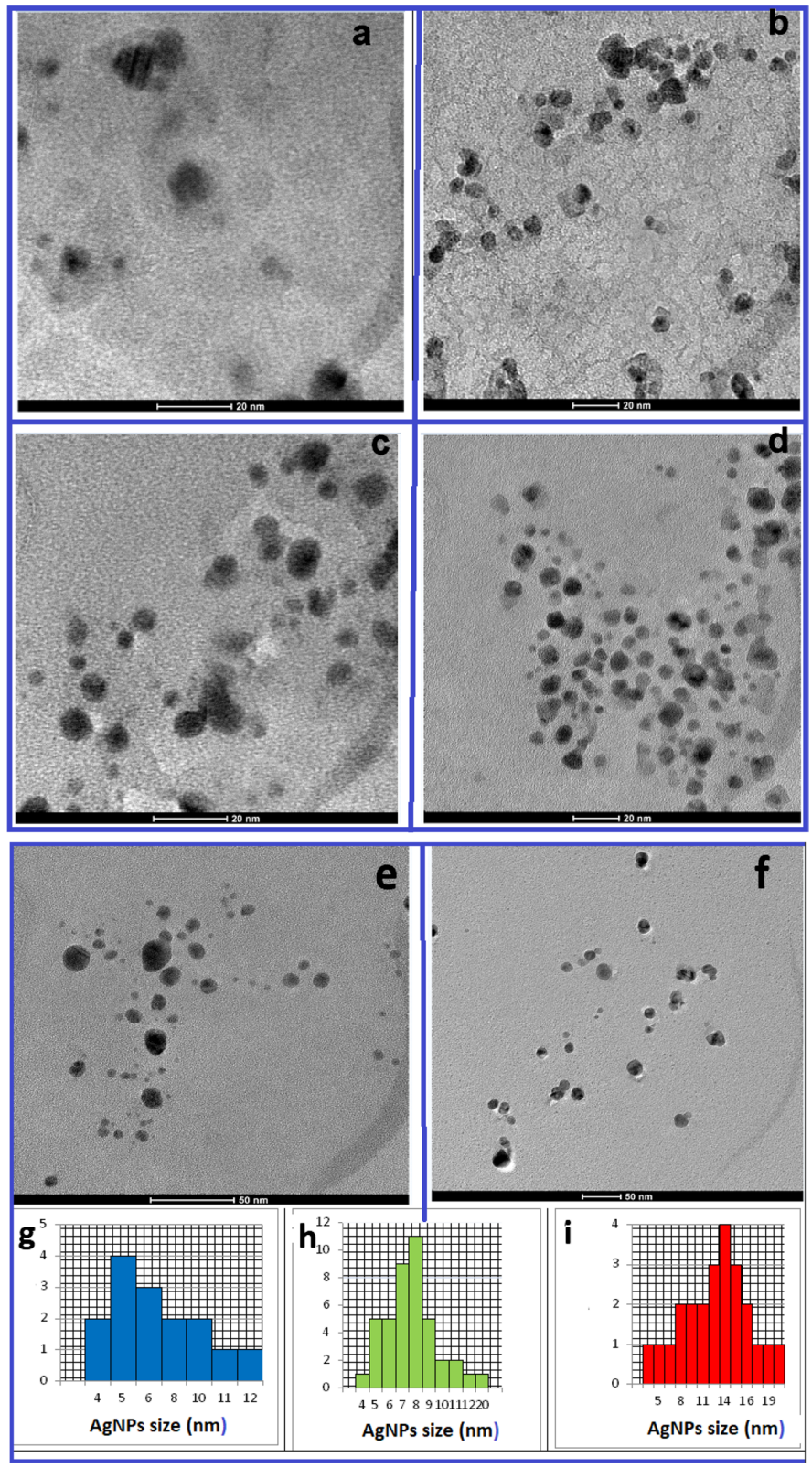

Fig. 2 TEM images obtained from nanocomposite samples irradiated by blue LED (**a**, **b**); green LED (**c**, **d**), and red LED (**e**, **f**) respectively. Some TEM images show relatively good dispersed pictures. Images **a**, **d**, and **f** were analyzed by ImageJ software and corresponding particle size distribution histograms are shown in g, h, and i respectively

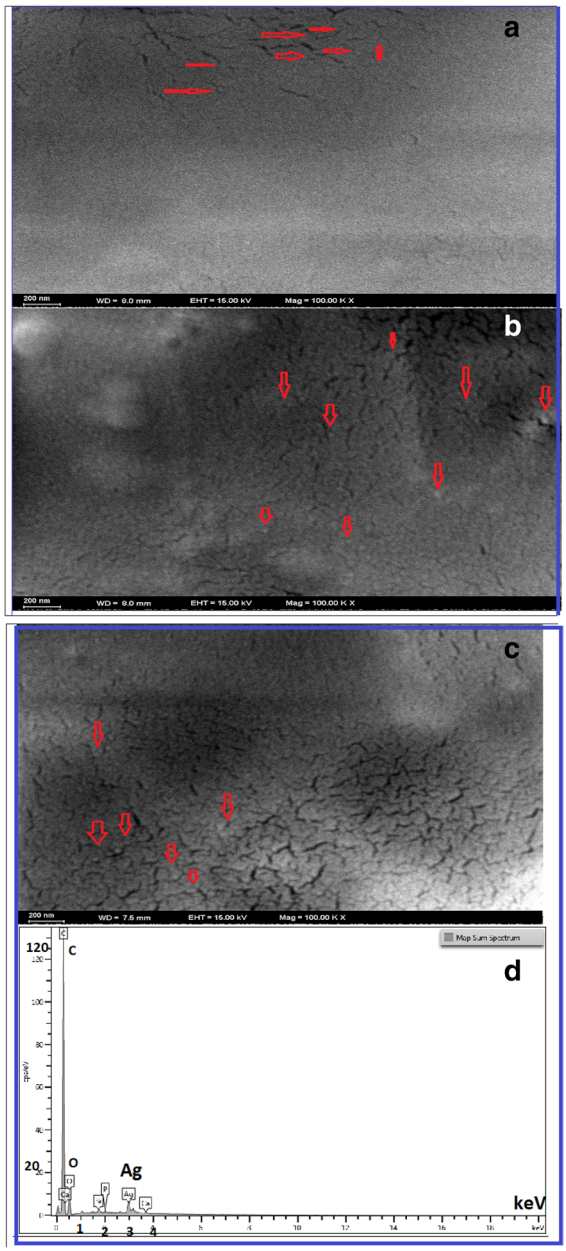

Fig. 3 SEM images of blue, green, and red LED-irradiated samples represented at **a**, **b**, **c** images and corresponding XPS map of the LED-irradiated sample at (**c**). SEM images have been taken at 100 × magnification and 200-nm scale

20° is assigned to the polysaccharide polymer structure of powdered nanocomposites, which is similar to the results reported in earlier studies [35, 36]. The synthesized AgNPs were characterized by UV–vis spectroscopy (Fig. 4c).

The UV–visible spectrum for all obtained suspensions reveals a maximum absorption band between 402 and 418 nm, which corresponds to the typical local surface plasmon resonance absorption of AgNPs [25, 26]. The sharp low-intensity peak at λmax = 402 nm (the blue spectra) belongs to AgNPs with average sizes 4–6 nm (samples irradiated by blue LED); the λmax values for the AgNPs obtained by green LED (average size 6–8 nm) and red LEDs (average size 12–14 nm) are detected at 409- and 418-nm wavelengths respectively. In red LED-irradiated sample, the absorption peak was slightly red shifted to a higher wavelength (418 nm), which indicated the increase in size of the AgNPs [33].

Infrared studies were carried out to ascertain the presence of the metal nanoparticles. FTIR spectra of the nanocomposite without any LED irradiation Fig. 5a and samples after visible LEDs stimulation are shown in Fig. 5b, c, and d.

The broad strong band ranging from 2962 to 3690 cm^{-1} appeared in all 4 spectra attributed to the O–H stretching vibrations of adsorbed water molecules [37]. For non-treated sample, peak was detected at 3360 cm^{-1}, while for all light-irradiated samples it was slightly shifted towards 3352 cm^{-1}. This may be due to O–H stretching and deformation, respectively assigned to the water adsorption on the metal surface [37, 38]. Moreover, increasing in intensity of these bands for irradiated samples evidenced that with visible LED-stimulated Ag ions can interact with hydroxyl and ester carboxylate groups of the polysaccharide nanocomposite and form AgNPs. The bands appearing around 668 cm^{-1} in all studied samples can be attributed to water molecules adsorption on the silver surface: metals generally give absorption bands in fingerprint region, i.e., below 1000 cm^{-1} arising from inter-atomic vibrations [38]. The strong bands appearing at 1637 cm^{-1} can be ascribed to C = O stretching vibration [39], C = C in alkenes [40], NH out-of-plane, and NH2 in plane [41, 42], and C = N groups [43]. The band at about 1637 cm^{-1} also often appears in montmorillonite spectra [44, 45] which can be assigned to ODA-MMT portion in studied nanocomposites. Upon irradiation with different light energy FTIR, spectra of the LED-irradiated nanocomposites (blue, green, and red traces) reveal almost similar bands and shifts. Interestingly, that identical results were observed in [46] upon gamma radiation carbon and carbon functionalized materials. The

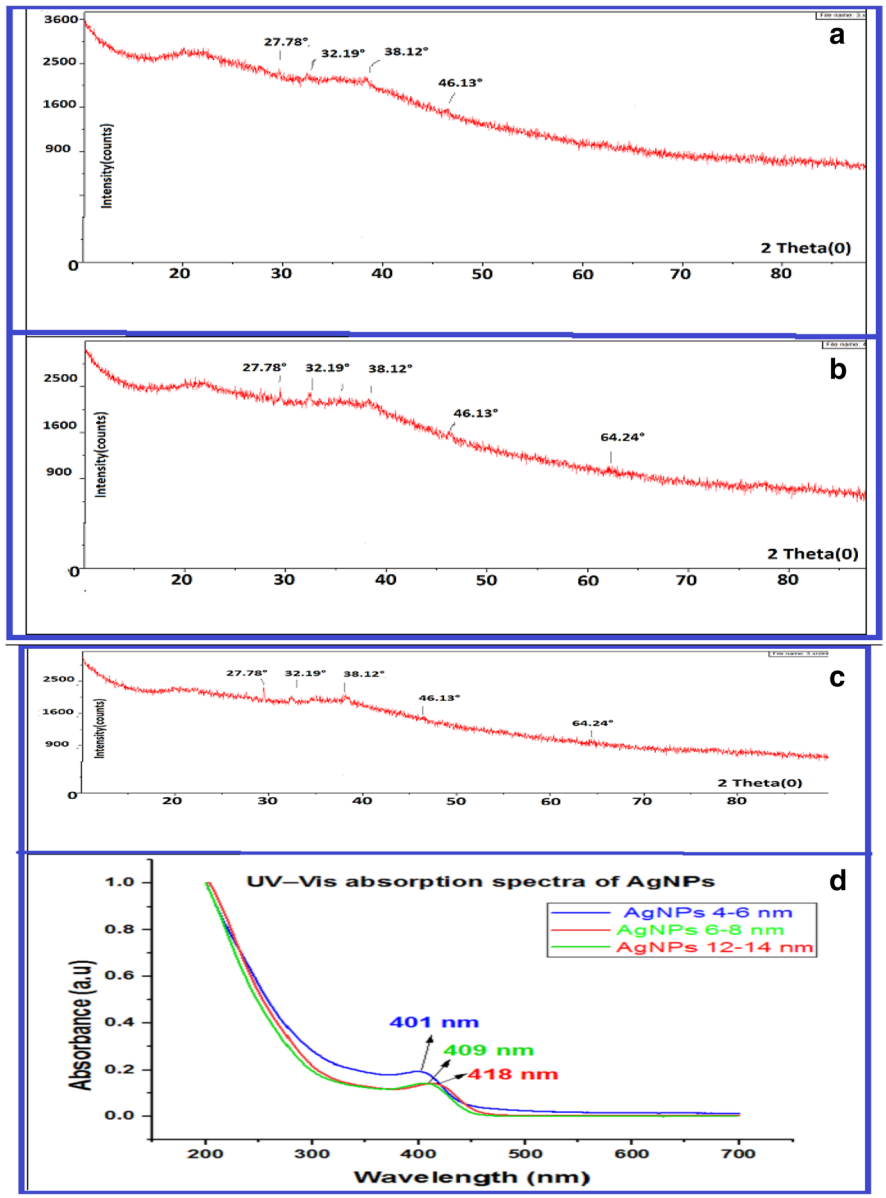

Fig. 4 **a** X-ray diffraction (XRD) pattern of blue LED; **b** green and **c** red LED-irradiated nanocomposites correspondingly; **d** UV–Vis absorption spectra, where SPR band for AgNPs irradiated by is blue LED (blue curve), by is (red curve) and by is green LED (green curve) respectively

similarity obtained FTIR spectra in our case may be due to that fact that Ag nanoparticles with spherical shape and an average particle size between 5.0 and 12.0 nm have an energy band around 5.6 and 5.1 eV [38]. As seen in Fig. 6c in our study, an average particle size proceeds between 5 and 14 nm and energy of used LEDs ranges from 5.04 to 7.04 eV which is enough for electronic transitions from the conduction to the valence band in all obtained AgNPs. Moreover, Kumar and coworkers [38] reported that the increase in particle size of the Ag nanoparticles leads to the decreased band gap energy which also in agreement with our findings.

Finding from the applied novel approach—real-time monitoring and quantifying the formation process of AgNPs

Figure 6a and b show a dependence of the normalized voltage signals from both photodiodes as the function of the time: the blue traces represented experimental data from the blue LED; the green and red traces

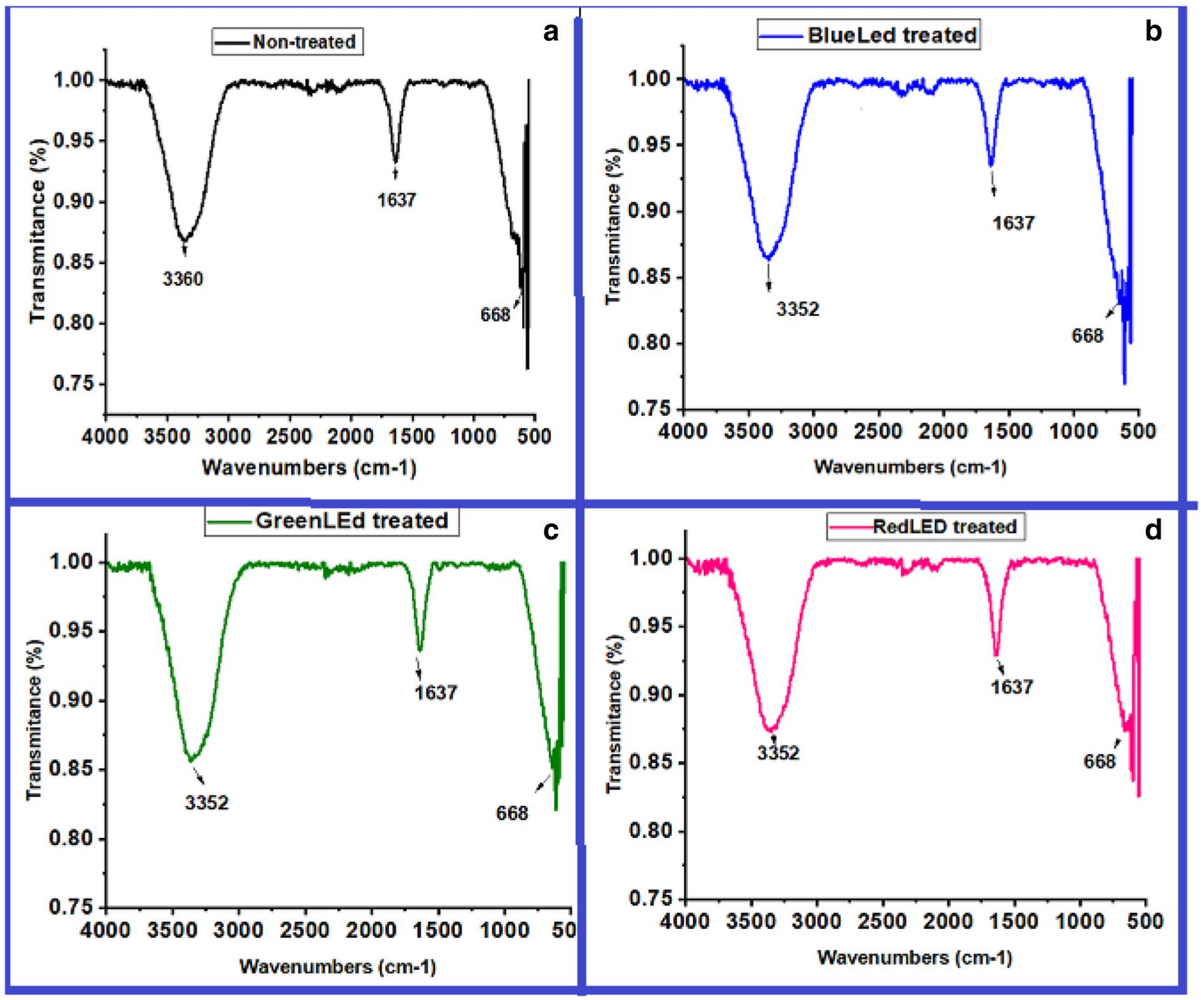

Fig. 5 FTIR spectra of the nanocomposite without any LED treatment **a** and samples after visible LED stimulation are shown in **b** blue LED-, **c**, green LED- and, **d** red LED-irradiated respectively

were data from the green and red LEDs respectively. In order to perform the measurements in similar intensities (0.6a.u.), several current correlations were implemented: blue LED has been used with a constant current 10 mA, and green and red LEDs with a constant current 50 mA and 30 mA correspondingly. Figure 2a and b show that the dependence for all measured data was well approximated by an exponential trace. The coefficients of the scattering traces (having the meaning of AgNP reducing speed) and as well as transmitted curves were changed in photon energy dependence manner. Indeed, it has been experimentally observed that the exponential coefficients decay rate k ($V = V_0 e^{-kt}$, where k = decay rate and t = photoreaction time) monotonically increases with the decrease of the photon wavelength (λ) (please also see Fig. 6c).

It is known that the classical light scattering theory for spherical particles based on the quasistatic (Rayleigh) approximation and the general Mie theory [47, 48]. Usually, Rayleigh scattering dominates when a wavelength is larger than a particle size. It is also known that for spherical particles in the Mie theory range tends to scatter in a mostly forward direction and scatters at a more sideways angle when Rayleigh theory predominates [49].

In our study, obtained AgNPs were much smaller than the light being used to interrogate (for

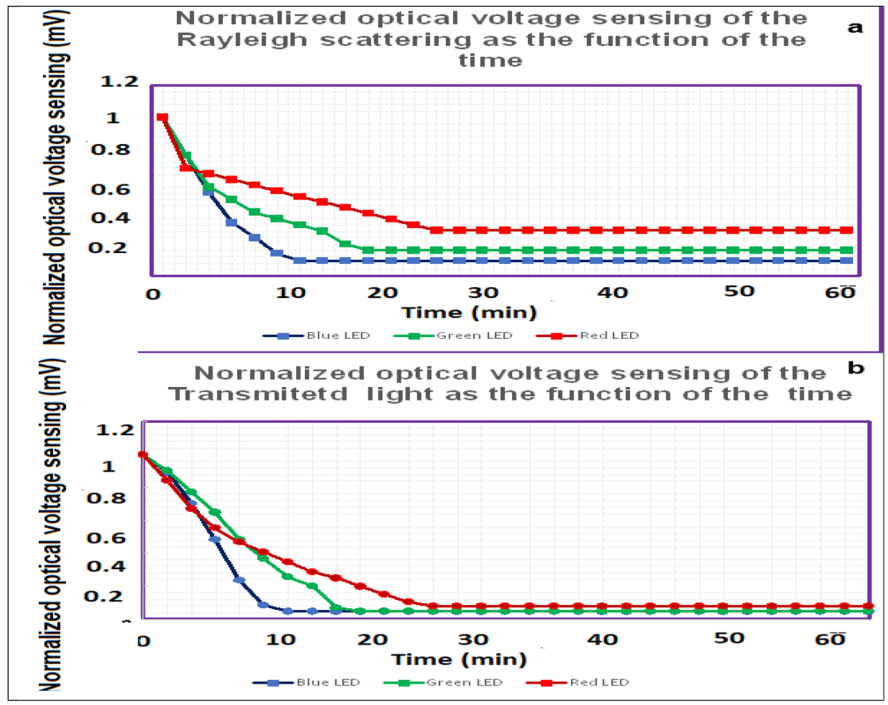

c

Photon Source LED	Photon Energy ; eV	Exp. coefficient k for Rayleigh scattering	Exp.coefficient; k for Transmitted	Optical density D	Photoreaction time (minutes)	AgNPs diameter (nm)
Blue	7.04	0.196	0.258	0.852	12	4-5
Green	6.11	0.102	0.168	0.681	16	7-8
Red	5.04	0.005	0.107	0.441	18	12-14

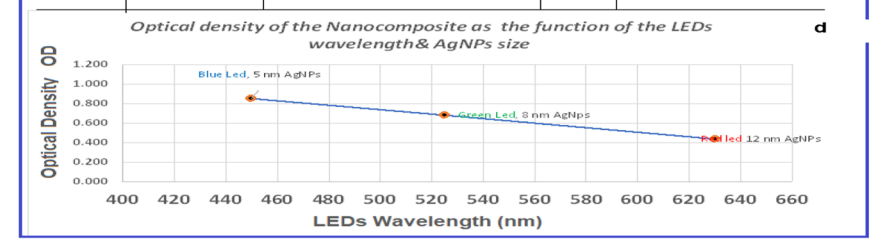

Fig. 6 **a** Normalized optical voltage signal from the Rayleigh scattering as the function of the time. **b** Normalized optical voltage signal from the transmitted light as the function of the time. In both figures, the blue traces correspond to the blue LED experiment data; green and red traces correspond to green and red LED data correspondingly; **c** optical density/extinction coefficient obtained using the Beer-Lambert law. **d** The optical density of the nanocomposite as the function of the LED wavelength and AgNP size (nanocomposition concentration and pathlength are constant)

the blue LED (450 nm), green LED (525 nm), and red LED (630 nm) and then Rayleigh scattering prevailed. We considered that the loss of light energy upon propagation through the solution of nanoparticles results only in the generation of heat and scattering. In this context, much of the light that treats the particle will scatter at some more "sideways" angle, which is detected by the photodiode in hole (1) (Fig. 1b). It is known that the absorption spectrum of small AgNPs is characterized by broadband covering the whole visible range and actually taking the major portion of the incoming light [50]. A high surface-to-volume ratio and, accordingly, a high percentage of atoms on the surface, are the main factors that play a role in the absorption of traveling light. In this connection, it can be said that 5 nm AgNPs, obtained by blue LED, will absorb light much more than 8- and 12-nm-sized AgNPs, which is confirmed by the traces of the transmitted light at Fig. 2b.

For a nanoparticle with dimensions much smaller than the wavelength of the propagating light, the absorption and scattering cross sections depend on 1/light wavelength and 1/light wavelength to the 4th-order dependence accordingly [49]. Figure 2a and b indicated that the voltage shown on photodiodes (1) and (2) (Fig. 1b) decreased over time and was characterized by a saturation plateau. The scattering light signal (Fig. 2a) was sensitive to the particle size; changes in voltage occur due to in situ generation and size reduction of the silver NPs. The fact that the voltage data collected from the photodiode on hole 1 changes with time can be used as the indicator of in-city reduction and generation of the AgNPs. It is well known that any variation in particle size, shape, or dielectric environment will change their scattering, absorption, and extinction responses [25, 26]. Moreover, researchers reported that the scattering intensity is increased by the increased light scattering from the dense ingested AgNP particles [51, 52]. The scattering cross section is a vital operator to understand the physical interaction between low-energy photons and the physical properties of the target particles [53]. In this sense, it is defined in as a collision of photons with targets AgNPs (either stationary or moving), and the probability for any given reaction to occur is in proportion to its cross section. Summarizing all of the above mentioned we can say that 12-nm-sized AgNps have more probability to scatters light then 8 nm; and it is exactly that the same provisions can apply to the 8 nm- and 5-nm-sized AgNPs. Experimentally archived data (Fig. 2a): red trace for 12-–14-nm-sized AgNPs, green for 6–8 and blue trace for 4–6 nm AgNps have confirmed the above written allegations. Moreover, the side-scatter signal shows a clear correlation with the size of the nanoparticles. It does not only describe the direct proportion of the scattering light portion to the scattered cross-section area, but also, the voltage stabilization indicates that the photosynthesis process is complete and AgNPs became stable over this time. Figure 6c summarizes all the above reference rates calculated for blue, green and red LEDs by using experimentally obtained data.

The wavelength of light is an important property that determines the nature of the light as well as its behavior with the surround environment. We have calculated energies of the photons using the classical Planck's equation $E = \mathrm{hc}/\lambda$ where λ is wavelength of the photon source and h where h is Planck's constant (Fig. 6c). We found that size factor of the AgNPs displayed increasing in the diameter of obtained NPs in a LED wavelength-dependent manner. The photoreduction of the AgNPs is in good agreement with photon energy values (Eblue > Egreen > E red).

The blue LED having photons energy 7.04 eV reduces AgNPs up to average size in range 4–6 nm in 12 min (Fig. 6a blue trace), while AgNPs obtained under influence of green and red LEDs with photon energies 6.11 and 5.04 eV respectively have average sizes 6–8 nm and 12–14 nm accordingly. (Fig. 6a green and red traces). It is known that for applications in which the attenuation/extinction coefficient and the pathlength are constant, the Beer-Lambert law can be used to proportionately correlate mixture concentration with optical density and vice versa. If a monochromatic (wavelength: λ nm) source of light of intensity, I0 is pointed at a 1-cm-thick specimen containing a mixture of c concentration; I is the intensity of the light that can transmit through this mixture, then the absorbance A or optical density at this wavelength is expressed according to the well-known Lambert–Beer law's as $A = \mathrm{OD} = \lg(I/I0) = \acute{\varepsilon}\mathrm{cl}$ where ε is the molar extinction coefficient, which has an inherent value for each chemical species and changes with wavelength [54]. When light passes through a mixture, attenuation of the light intensity occurs by two mechanisms: in a homogeneous, single-phase solution, only absorbance contributes significantly to attenuation; in suspensions containing mixtures of two or more phases, like in our case, light scattering due to difference in refractive index and the shape of this index mismatch also contribute to light attenuation [55]. The Beer-Lambert law only applies rigorously to single-phase solutions; however, certain assumptions and approximations allow the Beer-Lambert law to be extended to systems that exhibit significant scattering [56]. Experimental data on optical density/extinction coefficient was obtained in this work using the Beer-Lambert law shown in Fig. 6c. Two features are immediately evident from the plot in Fig. 6d. First, the values obtained by fitting our experimental voltage sensing to the Beer-Lambert law are in a very good agreement with the existing literature [25, 26, 57, 58]. Obtained results confirm size-depending behavior of the extinction coefficient for AgNPs. The second feature on Fig. 6d is that the value of optical density decreases with increase of the wavelength of the light source. LED wavelength

changes are result in a proportional change in optical density values as well as AgNPs sizes for all 3 identical concentrations mixtures.

Antimicrobial activity results

In this study, our group investigated the inhibitory concentrations of 3 different AgNPs on the test microorganisms for the first time. The antibacterial and antifungal potentials of AgNPs were determined using the disc diffusion method at various concentrations of AgNPs in the range of 2.5–0.001 mg/mL and reported in Table 2 and Fig. 7. Our finding revealed that the size of the inhibition zone of AgNPs was basically determined by their concentration. The results of the antibacterial and antifungal tests showed that the highest inhibition zone diameter occurred at 2.5 mg/mL concentration for all AgNPs in all test microorganisms. On the other hand, the minimum inhibition concentration for all AgNPs against test microorganisms was evaluated for each microorganism separately.

Considering the antibacterial activity results for *E. faecalis* 29212 (Table 2 and Fig. 7), the highest zone diameter was recorded at 16.16 ± 0.20 mm for the highest concentrations in blue LED AgNPs. Furthermore, the minimum inhibitory concentration was determined at 0.05 mg/mL with an 11.10 ± 0.17 mm zone diameter for blue LED AgNP. Evaluating the antibacterial activity of green LED AgNP and red LED AgNPs for *E. faecalis* 29212, the antibacterial activities were discovered as the largest inhibition zone diameters at initial concentrations (green LED AgNP with 16.13 ± 0.23 mm and red LED AgNP with 16.06 ± 0.11 mm) and the minimum inhibitory concentrations were detected at 0.05 mg/mL concentration for both AgNPs against *E. faecalis* 29212 (all concentrations inhibition zone diameter value shown in Table 2).

When *E. coli* 25922 results were examined, blue LED AgNP displayed the largest inhibition zone at the highest concentration with a 14.06 ± 0.30 mm diameter (Table 2 and Fig. 7). Besides, the minimum inhibitory concentration of blue LED was stated at 0.05 mg/mL. On the other hand, green LED AgNPs showed the lowest inhibitory concentration for *E. coli* 25922 was determined at 0.01 mg/mL with a 9.10 ± 0.17 mm zone diameter. As for red LED AgNPs, the minimum inhibitory concentration was

Table 2 Antimicrobial activity results of Green Led AgNP, Blue LED AgNp, and Red LED AgNPs disc diffusion results of various concentrations. The results were given as inhibition zone diameter using millimeter (mm) unit for displaying radius of inhibition zone

	Green Led AgNP					Blue Led AgNP					Red Led AgNP				
	2.50	0.5	0.1	0.05	0.01	2.50	0.5	0.1	0.05	0.01	2.50	0.5	0.1	0.05	0.01
E. faecalis 29212	16.13 ± 0.23	14.30 ± 0.30	13.13 ± 0.15	11.16 ± 0.28	0	16.16 ± 0.20	14.20 ± 0.17	13.03 ± 0.05	11.10 ± 0.17	0	16.06 ± 0.11	12.23 ± 0.32	12.10 ± 0.17	12.10 ± 0.36	0
E.coli 25922	13.33 ± 0.57	12.06 ± 0.40	11.13 ± 0.23	11.16 ± 0.28	9.10 ± 0.17	14.06 ± 0.30	10.43 ± 0.37	10.13 ± 0.23	10.36 ± 0.32	0	13.16 ± 0.28	12.40 ± 0.36	12.20 ± 0.20	12.16 ± 0.28	7.30 ± 0.30
P. aeruginosa 27853		13.16 ± 0.37	12.13 ± 0.32	11.33 ± 0.35	8.16 ± 0.28	16.06 ± 0.20	13.10 ± 0.36	12.23 ± 0.25	12.20 ± 0.17	0	15.20 ± 0.34	14.10 ± 0.26	11.20 ± 0.26	11.26 ± 0.25	0
C. albicans 10231	12.40 ± 0.69	10,06 ± 0.11	8.16 ± 0.28	8.30 ± 0.26	0	11.23 ± 0.25	11.10 ± 0.45	9.06 ± 0.40	7.13 ± 0.23	0	14.20 ± 0.20	11.00 ± 0.20	9.10 ± 0.36	7.13 ± 0.23	0

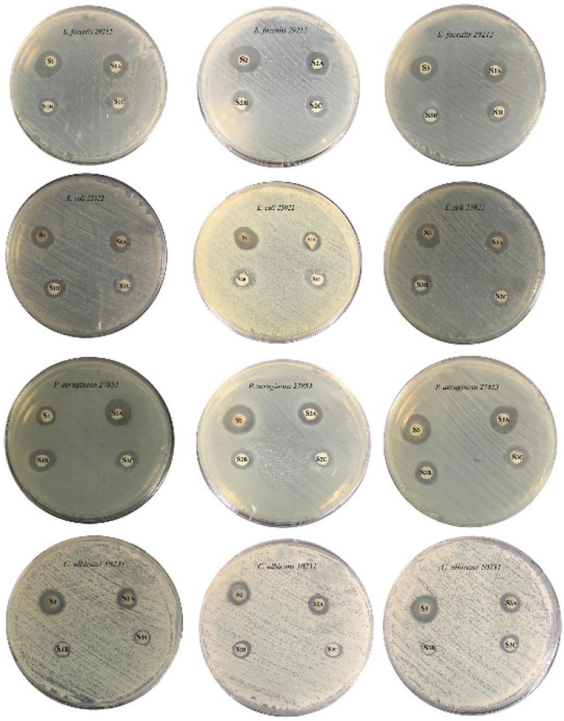

Fig. 7 Antimicrobial activity results based on disc diffusion method with various concentrations of green, blue, and red LED AgNPs against test microorganisms

determined at 0.01 mg/mL with a 7.30 ± 0.30 mm zone diameter.

A concentration-dependent effect was observed against *P. aeruginosa* 27853 for each AgNPs (Table 2 and Fig. 7). The biggest inhibition zone diameter of 16.06 ± 0.20 mm was determined for blue LED AgNPs at the highest concentration. The inhibition value of the different concentrations of blue LED AgNPs changed depending on changing the concentration value and recorded a minimum inhibitory concentration of 12.20 ± 0.17 mm at 0.05 mg/mL. However, the lowest inhibition concentration for *P.aeruginosa* 27853 was found at 0.01 mg/mL with an 8.16 ± 0.28 mm zone diameter in green LED AgNPs. As regards red LED AgNPs results, the minimum inhibitory concentration was assessed at 0.05 mg/mL with an 11.26 ± 0.25 mm zone. The antifungal results of *C. albicans* 10231 indicated that inhibition results were based on AgNP concentrations (given in Table 1 and Fig. 7). Interestingly, the antifungal test for yeast was non-ordinary besides the antibacterial test: the red LED-irradiated AgNPs showed the largest inhibition for the initial three dilutions followed by green LED-irradiated and blue LED-irradiated AgNPs. Statistical analysis revealed that antimicrobial activity results showed a significant difference in various concentrations of all AgNPs ($p < 0.05$).

Li et al. [59] used pure CMC-coated AgNP against *E. coli* and *S. aureus* and found the inhibition zone diameters were around 8.03 and 14.93 mm. These results were obtained at fixed $AgNO_3$ concentration (at 0.5 mM) but different concentrations of CMC. In other work, Basuny et al. [60] carried out an experiment with AgNPs obtained from 5.0 mM $AgNO_3$, and embedded in CMC against *E. coli* NCTC 10416, *P. aeruginosa* NCIB 9016, *B. subtilis* NCIB 3610, *S. aureus* NCTC 7447, and *C. albicans* IMRU 3669. According to this study, the antimicrobial activities of AgNP embedded in CMC and pure CMC were investigated, and it was found that AgNP embedded in CMC had antimicrobial activity against all test microorganisms. The inhibition zones for all test microorganisms were measured as *E. coli* NCTC 10416 14 mm, *P. aeruginosa* NCIB 9016 16 mm, *B. subtilis* NCIB 3610 13.5 mm, *S. aureus* NCTC 7447 11 mm, and *C. albicans* IMRU 3669 16 mm. In this study, we carried out the antimicrobial activity with three different nanoparticles that have similar sizes such as 4–6 nm and 6–8 nm for blue and green LED. Our results showed that inhibition depended on the dosage of nanoparticles, in particular, bacterial strains (*E. faecalis* 29212, *P. aeruginosa* 27853, and *E. coli* 25922) displayed similar antimicrobial activity patterns. Recent research pointed out that particle size and dose are important for the strength of antimicrobial activity. Small silver nanoparticles were found more effective than bigger-size silver nanoparticles also dose-dependent activity was shown on *E. coli* MTCC 443 and *S. aureus* NCIM 5201 [61]. From this point of view, the results for bacterial strains support the idea of the size and dose-dependent activity of silver nanoparticles.

Silver nanostructures (particles, composites, etc.) are well-known antimicrobial agents used in various areas to eliminate pathogens from biotic and abiotic surfaces. In particular, the development of biomaterials in medical applications using silver nanostructures has been distinguished by their strong antimicrobial properties. Hence, conducted studies have focused on mechanisms or interactions of AgNPs with microorganisms. One of these studies reported by Sondi et al.

unveiled that AgNP affected *E.coli* through damaging cell walls called pits on the bacterial cell wall [62]. The pits collected AgNPs on the cell wall and caused the death of bacteria with increased cell permeability. Known mechanisms for the antimicrobial activities of AgNPs include disrupting the function of respiratory chain reactions by oxidative damage and lipid peroxidation. Also, AgNPs bind with the sulfur and phosphorus groups of DNA and interrupt the transcription and translation of proteins. *P. aeruginosa* is an example of lipid oxidation by AgNPs, and AgNPs engender DNA damage and termination of life for bacteria [63]. Besides, by changing the bacterial growth phase timing (extension of the lag phase), AgNPs could have lytic activity against *E. faecalis* [64].

Based on the literature review above, the antimicrobial potency data obtained in our study agrees well with reported results. On the other hand, our literature survey showed that antibacterial activity studied in this work pathogenesis at various concentrations of AgNPs using disc diffusion method has never been attempted before. According to the findings of this study, all AgNPs have great potential as antimicrobial agents against test microorganisms that were used. Furthermore, its antimicrobial activities with different concentrations of AgNPs continued and thus gave an opportunity for usage at a lower dosage than in the beginning. In this study, the minimum inhibitory concentration value was detected at 0.05 mg/mL for *E.faecalis* and *C. albicans* in blue, green, and red LED-irradiated AgNPs. However, the minimum inhibitory concentration of green LED AgNPs was detected as 0.01 mg/mL for *E. coli* and *P. aeruginosa*. Regarding the minimum inhibitory concentration of blue and red LED AgNPs, 0.05 mg/mL was determined for *E. coli* and *P. aeruginosa*. The difference in minimum inhibitory concentration for test microorganisms could be affiliated with the cell wall's structure and the surface's ionic charge. Obtained data indicates that blue, green, and red LED AgNPs are candidates for new-generation antimicrobial agents against strong pathogens.

Conclusion

The first scattering light-sensitive device was designed, fabricated, and successfully tested for formation and real-time monitoring AgNPs in biopolymer media. In this work, synthesis and size distribution of AgNPs and their antimicrobial activity were studied owing to the changes in LEDs energy and recording of photodiode voltage versus time. It can be inferred that a photon energy is crucial for the reaction time and size distribution small-sized spherical nanoparticles. The blue LED having photons energy 7.04 eV reduces AgNPs up to average size in range 4–6 nm in 12 min, while AgNPs obtained under influence of green and red LEDs with photon energies 6.11 and 5.04 eV respectively have average sizes 6–8 nm and 12–14 nm accordingly. The successful formation of AgNPs additionally was examined using UV–Vis, SEM, XPS, XRD, FTIR, and TEM techniques. The prepared silver nanoparticles showcased persuasive antimicrobial activity against both gram-positive and gram-negative bacterial strains and yeast. AgNPs proved antimicrobial activity against *E. coli* 25922, *E. sfaecalis* 29212, *P. aeruginosa* 27853, and *C. albicans* 10231 with different inhibition zone diameters at different concentrations. All antimicrobial tests treated with AgNPs demonstrated a dose-dependent inhibition effect on the studied microorganisms. The minimum inhibitory concentration value was detected at 0.05 mg/mL for *E. faecalis* and *C. albicans* for all studied sized AgNPs. The antibacterial for all examined bacteria shows that AgNPs synthesized by blue LED (4–6 nm) reveal the largest inhibition zone (btw16–11 mm diameter) while antifungal test shows that AgNPs (11–12 nm) synthesized by red LED reveals largest inhibition zone.

Declarations

Conflict of interest The authors declare no competing interests.

References

1. Ahmad MZ, Akhter S, Jain GK, Rahman M, Pathan SA, Ahmad FJ, Khar RK (2010) Metallic nanoparticles: technology overview & drug delivery applications in oncology. Expert Opin Drug Deliv 7(8):927–42
2. Bunyatova U, Hammouda MB, Zhang J (2021) Novel light-driven functional AgNPs induce cancer death at extra low concentrations. Sci Rep 11:13258
3. Rai M, Ingle AP, Birla S, Yadav A, dos Santos CA (2016) Strategic role of selected noble metal nanoparticles in medicine. Crit Revi Microbiol 42(5):696–719
4. Rzayev Z, Bunyatova U, Lowell J, Shen W, Thomay T, Carwright A (2018) Novel Ag-carried CMC/functional

copolymer/ODA-Mt wLED-treated NC and their responses to brain cancer cells. Mater Sci Eng, C 8(11):463–476
5. Yang Y, Matsubara S, Xiong L (2007) Solvothermal synthesis of multiple shapes of silver nanoparticles and their SERS properties. J Phys Chem 111:9095–9104
6. Salkar RA, Jeevanandam P, Aruna ST, Koltypin Y, Gedanken A (1999) The sonochemical preparation of amorphous silvernanoparticles. J Mater Chem 9:13
7. Lee PC, Merisel D (1982) Adsorption and surface-enhanced Raman of dyes on silver and gold sols. J Phys Chem 86:3391–3395
8. Simakin AV, Voronov VV, Kirichenko NA, Shafeev GA (2004) Nanoparticles produced by laser ablation of solids in liquidenvironment. Appl Phys A 79:1127
9. Naik RR, Stringer SJ, Agarwal G, Jones SE, Stone O (2002) Biomimetic synthesis and patterning of silver nanoparticles. Nat Mater 1:169–172
10. Singh J, Dutta T, Kim KH et al (2018) 'Green' synthesis of metals and their oxide nanoparticles: applications for environmental remediation. J Nanobiotechnol 16:84. https://doi.org/10.1186/s12951-018-0408-4
11. Iqtedar M, Aslam M, Akhyar M, Shehzaad A, Abdullah R, Kaleem A (2019) Extracellular biosynthesis, characterization, optimization of silver nanoparticles (AgNPs) using Bacillus mojavensis BTCB15 and its antimicrobial activity against multidrug resistant pathogens. Prep Biochem Biotechnol 49(2):136–142. https://doi.org/10.1080/10826068.2018.1550654
12. Zia R, Riaz M, Faroo N, Qamar A, Anjum S (2018) Antibacterial activity of Ag and Cu nanoparticles synthesized by chemical reduction method: a comparative analysis. Mater Res Express 5:7
13. Rzayev Z, Erdonmez D, Erkan K, Simsek M, Bunyatova U (2015) Functional copolymer/organo-MMT Nanoarchitectures. XXII. Fabrication and characterization of antifungal and antibacterial poly (vinyl alcohol-co-vinyl acetate/ODA-MMT/AgNPs nanofibers and nanocoatings by e-spinning and c-spinning methods. Int J Polym Mater 64:267–278
14. Marambio-Jones C, Hoek EMV (2010) A review of the antibacterial effects of silver nanomaterials and potential implications for human health and the environment. J Nanopart Res 12:1531–1551
15. Chouhan N (2018) Silver nanoparticles: synthesis, characterization and applications, book. In Silver Nanoparticles: Fabrication, Characterization and Applications. IntechOpen. https://doi.org/10.5772/intechopen.75611
16. Xu L, Wang YY, Huang J, Chen CY, Wang ZX, Xie H (2020).Silver nanoparticles: synthesis, medical applications and biosafety. Theranostics 10(20):8996–9031. https://doi.org/10.7150/thno.45413
17. Altinsoy BD, Karatoprak GS, Ocsoy I (2019) Extracellular directed ag NPs formation and investigation of their antimicrobial and cytotoxic properties c. Saudi Pharm J 27:9–16
18. Akhtar M, Panwar J, Yun YS (2013) Biogenic synthesis of metallic nanoparticles by plant extracts. ACS Sustain Chem Eng 1:591–602
19 Emam HE, El-Bisi MK (2014) Merely Ag nanoparticles using different cellulose fibers as removable reductant. Cellulose 21(6):4219–4230
20. Trader DJ, Carlson EE (2012) Chemoselective hydroxyl group transformation: an elusive target. Mol Biosyst 8(10):2484–2493
21 Shaikh WA, Chakraborty S, Owens G, Islam RU (2021) A review of the phytochemical mediated synthesis of AgNP (silver nanoparticle): the wonder particle of the past decade. Appl Nanosci 11(11):2625–2660. https://doi.org/10.1007/s13204-021-02135-5
22. Wang WS, Du H, Wang RX, Wen T, Xu AW (2013) Heterostructured Ag3PO4/AgBr/Ag plasmonic photocatalyst with enhanced photocatalytic activity and stability under visible light. Nanoscale 5(8):3315–3321. https://doi.org/10.1039/c3nr00191a
23. Tighe-Neira R, Carmora E, Recio G, Nunes-Nesi A, Reyes-Diaz M, Alberdi M, Rengel Z, Inostroza-Blancheteau C (2018) Metallic nanoparticles influence the structure and function of the photosynthetic apparatus in plants. Plant Physiol Biochem 130:408–417
24 Han P, Martens W, Waclawik E, Sarina S, Zhu HY (2018) Metal nanoparticle photocatalysts: Synthesis, characterization, and application. Part Part Syst Charact 35(6):17004891–16
25. Wiley BJ et al (2006) Maneuvering the surface plasmon resonance of silver nanoparticles through shape- controlled synthesis. J Phys Chem B 110(32):15666–15675
26. Noginov MA et al (2007) Te efect of gain and absorption on surface plasmons in metal nanoparticles. Appl Phys B 86:455–460
27. Maretti L, Billone PS, Liu Y, Scaiano JC (2009) Facile photochemical synthesis and characterization of highly fluorescent silver nanoparticles. J Am Chem Soc 131(39):13972–13980. https://doi.org/10.1021/ja900201k
28. Oliveira E, Santos HM, Garcia-Pardo J, Diniz M, Lorenzo J, Rodríguez-González B, Capelo JL, Lodeiro C (2013) Synthesis of functionalized fluorescent silver nanoparticles and their toxicological effect in aquatic environments (Goldfish) and HEPG2 cells. Front Chem 5(1):29. https://doi.org/10.3389/fchem.2013.00029
29. Meng Y (2015) A Sustainable Approach to Fabricating Ag Nanoparticles/PVA Hybrid nanofiber and its catalytic activity. Nanomaterials (Basel) 5(2):1124–1135. https://doi.org/10.3390/nano5021124
30. Anju K, AnithaJegadeeshwari L, Nagendra Gandhi N (2018) optimization of green synthesized silver nanoparticles from caralluma umbellata. Int J Appl Pharm 10(4):103
31. Ashraf H, Anjum T, Riaz S, Naseem S (2020) Microwave-assisted green synthesis and characterization of silver nanoparticles using melia azedarach for the management of fusarium wilt in tomato. Front Microbiol 10(11):238. https://doi.org/10.3389/fmicb.2020.00238.PMID:32210928;PMCID:PMC7076090
32. Bandla M, Abbavaram BR, Kokkarachedu V, Sadiku RE (2017) Silver nanoparticles incorporated within intercalated clay/polymer nanocomposite hydrogels for antibacterial studies. Polym Compos 38:E16–E23. https://doi.org/10.1002/pc.23963
33. Shameli K, Bin Ahmad M, Zargar M, Yunus WM, Ibrahim NA, Shabanzadeh P, Moghaddam MG (2011) Synthesis and characterization of silver/montmorillonite/chitosan bionanocomposites by chemical reduction method and their antibacterial activity. Int J Nanomedicine 6:271–84

34. Aziz SB at al (2019) Structural, thermal, morphological and optical properties of PEO filled with biosynthesized Ag nanoparticles: New insights to band gap study. Results Phys 13. https://doi.org/10.1016/j.rinp.2019.102220
35. Brza MA (2020) at al The study of EDLC device with high electrochemical performance fabricated from proton ion conducting pva-based polymer composite electrolytes plasticized with glycerol. Polymers (Basel) 12(9):1896
36. Hamsan MH, Shukur MF, Aziz SB, Kadir MFZ (2019) Dextran from Leuconostoc mesenteroides-doped ammonium salt-based green polymer electrolyte. Bull Mater Sci 42:57
37. A Mohammadi, Barikani M, Barmar M (2015) Synthesis and investigation of thermaland mechanical properties of in situ prepared biocompatible Fe3O4/polyurethane elastomer nanocomposites. Polym Bull 72(2):219–234. https://doi.org/10.1007/s00289-014-1268-1
38. Kumar H at al (2013) Structural characterization of silver nanoparticles synthesized by micro emulsion route. Int J Eng Innov Technol (IJEIT) 3(3):2277–3754. ISO 9001:2008
39. Yasmeen S, Kanti Kabiraz M, Saha B, Rakibul Qadir M, Abdul Gafur M, Md Masum S (2015) Chromium (VI) ions removal from tannery effluent using chitosan-microcrystalline cellulose composite as adsorbent. Int Res J Pure Appl Chem 10(4):1–14. https://doi.org/10.9734/IRJPAC/2016/23315
40. http://users.wfu.edu/wrightmw/chm122/handouts/IRFunGroup.pdf]
41. Applications of Infrared spectroscopy in biochemistry, Biology, and Medicine pp 165–172. Springer New York, NY. https://doi.org/10.1007/978-1-4684-1872-9
42. Chrzanowska E, Gierszewska M, Kujawa J, Raszkowska-Kaczor A, Kujawski W (2018) Development and characterization of polyamide-supported chitosan nanocomposite membranes for hydrophilic pervaporation. Polymers (Basel) 10(8):868
43. Bagleyt GK at al (1982) Fourier transform infrared difference. spectroscopy of bacteriorhodopsin and its photoproducts. Biophysics 79(16):4972–4976. https://doi.org/10.1073/pnas.79.16.4972
44. Zeng QH, Wang DZ, Yu AB, Lu GQ (2002) Synthesis of polymer-montmorillonite nanocomposites by in situ intercalative polymerization. Nanotechnology 13(5):549–553
45. Hayati-Ashtiani M (012) Use of FTIR spectroscopy in the characterization of natural and treated nanostructured bentonites montmorillonites. Part Sci Tech 30(6):553–564. https://doi.org/10.1080/02726351.2011.615895
46. Synthesis, technology and applications of carbon nanomaterials (2019). Elsevier. https://doi.org/10.1016/C2017-0-03040-9
47. Rayleigh L (1871) On the scattering of light by small particles. Philos Mag 41:447–454
48. Wang ZB, Luk'yanchuk BS, Hong MH, Lin Y, Chong TC (2004) Energy flow around a small particle investigated by classical Mie theory. Phys Rev B 7003541. https://doi.org/10.1103/PhysRevB.70.035418
49. van de Hulst HC (1981) light scattering by small particles. Dover, New York 15. https://doi.org/10.1002/actp.1984.010350426
50. Hainga M et al (2016) Absorption and scattering cross-section extinction values of silver nanoparticles. Opt Mater 58:439–444
51. Song JE, Park JH, La JA, Park S, Jeong MK, Cho EC (2016) Use of fluorescence signals generated by elastic scattering under monochromatic incident light for determining the scattering efficiencies of various plasmonic nanoparticles. Analyst 15. https://doi.org/10.1039/C6AN00399K
52. Helmlinger J, Sengstock C, Groß-Heitfeld C, Mayer C, Schildhauer TA, Koller M, Epple M (2016) Silver nanoparticles with different size and shape: equal cytotoxicity, but different antibacterial effects. RSC Adv 6(22):18490–18501. https://doi.org/10.1039/C5RA27836H
53. Marghany M in synthetic aperture radar imaging mechanism for oil spills, quantize of scattering theory
54. Itagaki H (2000). Experimental methods in polymer science. Modern Methods in Polymer Research and Technology. A volume in Polymers, Interfaces and BiomaterialsBook pp 155–260.https://doi.org/10.1016/B978-0-08-050612-8.50009-X
55. Swanson NL, Billard BD, Gennaro TL (1999) Limits of optical transmission measurements with application to particle sizing techniques. Appl Opt 38:5887–5893
56. Myers JA, Curtis BS, Curtis WR (2013) Improving accuracy of cell and chromophore concentration measurements using optical density. BMC Biophysics 6:4
57. Paramelle D, Sadovoy A, Gorelik S, Free P, Hobley J, Fernigb DG (2014) Rapid method to estimate the concentration of citrate capped silver nanoparticles from UV-visible light spectra. The Analyst 19. https://doi.org/10.1039/c4an00978a
58. Free P, Paramelle D, Bosman M, Hobley J, Fernig DG (2012) Synthesis of silver nanoparticles with monovalently functionalized self-assembled monolayers. Chem 65:275–282
59. Li G, Liu L, Sun Y, Liu H (2018) Ecofriendly synthesis of silver–carboxy methyl cellulose nanocomposites and their antibacterial activity. J Clust Sci 29:1193–1199. https://doi.org/10.1007/s10876-018-1426-y
60. Basuny M, Ali IO, Abd EA, Bakr MF, Salama TM (2015) A fast green synthesis of Ag nanoparticles in carboxymethyl cellulose (CMC) through UV irradiation technique for antibacterial applications. J Sol-Gel Sci Technol 75:530–540. https://doi.org/10.1007/s10971-015-3723-3
61. Agnihotri S, Mukherji S, Mukherji S (2014) Size-controlled silver nanoparticles synthesized over the range 5–100 nm using the same protocol and their antibacterial efficacy. RSC Adv 4:3974
62. Sondi I, Salopek-Sondi B (2004) Silver nanoparticles as antimicrobial agent: a case study on E. coli as a model for Gram-negative bacteria. J Colloid Interface Sci 275(1):177–182

63. Liao S, Zhang Y, Pan X, Zhu F, Jiang C, Liu Q, Cheng Z, Dai G, Wu G, Wang L, Chen L (2019) Antibacterial activity and mechanism of silver nanoparticles against multidrug-resistant Pseudomonas aeruginosa. Int J Nanomed 1469–1487. https://doi.org/10.2147/IJN.S191340
64. Rajasekhar R, James B, Devadathan A, Soman S, Sebastian VM, Sathyan M (2022) An in vitro evaluation of antibacterial and smear layer removal efficacy of silver nanoparticles as final irrigant against enterococcus faecalis. World J Dent 13(2). https://doi.org/10.5005/jp-journals-10015-1913